

Failure assessment of eccentric circular holes under compressive loading

*Original*

Failure assessment of eccentric circular holes under compressive loading / Ferriani, F., Sapora, A., Estevez, R., Doitrand, A.. - In: INTERNATIONAL JOURNAL OF FRACTURE. - ISSN 0376-9429. - (2024). [10.1007/s10704-024-00805-3]

*Availability:*

This version is available at: 11583/2993218 since: 2024-10-09T14:34:41Z

*Publisher:*

Springer

*Published*

DOI:10.1007/s10704-024-00805-3

*Terms of use:*

This article is made available under terms and conditions as specified in the corresponding bibliographic description in the repository

*Publisher copyright*

(Article begins on next page)



# Failure assessment of eccentric circular holes under compressive loading

Francesco Ferrian · Alberto Sapora · Rafael Estevez · Aurélien Doitrand

Received: 8 April 2024 / Accepted: 29 June 2024  
© The Author(s) 2024

**Abstract** The present work aims to investigate the failure size effect on flattened disks containing an eccentric circular hole under mode I loading conditions. For this purpose, uniaxial compression tests are carried out on polymethyl methacrylate (PMMA) samples with holes. Depending on the hole radius and eccentricity, the energy release rate is either an increasing or decreasing function of the crack length, thus affecting the stability of crack propagation. Experimental results are interpreted and discussed through the coupled stress and energy criterion of Finite Fracture Mechanics. The approach lies on the assumption of a finite crack advance and it is implemented through the numerical estimation of the stress field and the Incremental Energy Release Rate functions. Finally, stability and crack speed propagation are discussed under the assumption of Linear Elastic Fracture Mechanics. Theoretical predictions reveal in agreement with experimental results thus

demonstrating that the Coupled Criterion effectively captures the failure condition.

**Keywords** Eccentric circular hole · Finite Fracture Mechanics · Size effect · Crack initiation · Stability

## 1 Introduction

Stress concentrators, such as flaws, holes or notches are present in a large number of engineering components and can strongly affect the structural strength. Indeed, acting as stress raisers, they decrease the load-bearing capacity, ultimately resulting in reducing the load span for mechanical integrity. Different approaches have been proposed in the last few decades to assess the crack initiation at stress concentrators. A preliminarily stress-based criterion was proposed by (Neuber 1936), who proposed the so-called Line Method. This criterion involved calculating a reference stress by averaging the stress field over a material unit, thus considering a finite volume. (Peterson 1938) simplified Neuber's approach by evaluating the reference stress at a given distance from the notch tip. (Taylor 2007), also inspired by the works of (Hashin 1996) and (Kim and Nairn 2000), formalized these approaches under the name of Theory of Critical Distances (TCD). The TCD criterion introduces a length parameter, which is a material property depending on the (squared) ratio between the fracture

---

F. Ferrian (✉) · A. Sapora  
Department of Structural, Geotechnical and Building  
Engineering, Politecnico di Torino, Turin, Italy  
e-mail: francesco.ferrian@polito.it

R. Estevez  
Université Grenoble-Alpes - CNRS UMR 5266, SIMaP,  
38000 Grenoble, France

A. Doitrand  
INSA-Lyon, Université Claude Bernard Lyon 1, CNRS,  
MATEIS, UMR5510, 69621 Villeurbanne, France

toughness  $K_{Ic}$  and the inherent strength, that can be considered equal to the ultimate tensile strength  $\sigma_c$  for very-brittle materials such as laminated composites (Whitney and Nuismer 1974) and ceramics (Taylor 2004). When the final failure occurs by propagation of pre-existing micro-defects or plastic deformation, the inherent strength assumes a value larger than  $\sigma_c$ . For polymers, the ratio between the inherent strength and  $\sigma_c$  typically is comprised between 1 and 2 ((Taylor 2007), (Cicero et al. 2012)). Many efforts have been conducted to provide a physical meaning to the critical distance, correlating it with some microstructural parameters, such as grain size or molecular scales (Taylor 2006), (Taylor 2007), (Marsavina et al. 2023). Furthermore, this length parameter was evaluated based on statistical models of defect evolution (Vedernikova et al. 2019). On the other hand, investigations by (Awerbuch and Madhukar 1985), (Pipes et al. 1979), and (Tan 1987) showed a dependence of the critical distance on other parameters, such as geometry characteristics. To address this issue, the Finite Fracture Mechanics (FFM) approach was introduced by coupling a stress requirement and an energy balance involving the Incremental Energy Release Rate (IERR) (Leguillon 2002) and (Cornetti et al. 2006). Unlike TCD, the coupled criterion does not require any length input parameter but enables determining the initiation crack length which depends on loading conditions and geometric features as well. FFM was applied to a wide range of structural configurations, providing accurate strength estimations. Focusing on the failure behavior of geometries containing a circular hole under uniaxial loading conditions, theoretical studies and experimental data were presented by (Li and Zhang 2006), (Sapora et al. 2018), (Leite et al. 2021), (Carrère et al. 2021). In such cases, the crack propagation is unstable. On the other hand, this is not always the case for biaxial loading conditions, as detected by (Sapora and Cornetti 2018) on the experimental results obtained by (Torabi et al. 2017). A comprehensive analysis of crack initiation from circular holes under biaxial loadings was presented by (Chao Correias et al. 2023) showing an agreement between FFM, Phase Field and Cohesive Zone Model predictions. As a matter of fact, using the formalism of (Weißgraeber et al. 2016), the energy release rate function can increase (positive geometry) or decrease (negative geometry) as the crack grows, depending on the loading conditions, radius values and

material anisotropy (Felger et al. 2017; Sakha et al. 2023). In the aforementioned works, because of the double symmetry of the structure, the propagation was always assumed to be symmetrical. For some geometries, this is not the case. Indeed, when considering a configuration presenting an eccentric circular hole or subjected to axisymmetric loading conditions, asymmetric crack patterns are expected to occur. In particular, (Rosendahl et al. 2017) investigated asymmetric crack initiation at open holes under tensile and in-plane bending loading. Furthermore, different asymmetric crack initiation scenarios were explored also by (Doitrand et al. 2021a, b) and by (Doitrand and Leguillon 2021) considering pore crack initiation near a free edge. Finally, the work of (Kurguzov and Kuznetsov 2024) investigated a Brazilian disk sample presenting a central circular hole with two edge radial cracks. In particular, this work analyzed the mixed mode loading induced by the rotation of the cracks relative to the vertical axis. Crack initiation in Brazilian disk specimens was also investigated in the framework of FFM by (Torabi et al. 2017) and (Doitrand and Sapora 2020).

The present study aims to investigate the brittle fracture of eccentric circular holes under pure mode I loading conditions experimentally and theoretically. For this purpose, compression tests are carried out on disk specimens made of PMMA and weakened by an eccentric circular hole. To catch the failure size effect, different hole radii are considered, and experimental results are compared with theoretical predictions provided by the FFM approach. The criterion is implemented numerically by parametric Finite Element Analyses (FEAs) through finite elements code, discussing asymmetric versus symmetric crack initiation scenarios.

Finally, crack propagation is investigated through an ultrahigh-speed acquisition camera. This setup enables the monitoring of crack length during the stable propagation phase and the determination of crack speed during the unstable one. Indeed, depending on the eccentricity and radius values, a locally positive/globally negative or locally negative/globally positive configuration can be obtained.

The paper is organized as follows: the experimental campaign on PMMA samples with a hole and related results will be presented in Sect. 2. The FFM criterion and its numerical implementation, considering different crack initiation scenarios, will be introduced in

Sect. 3. Section 4 will show the comparison between experimental results and strength estimations, together with considerations upon crack propagation stability. Finally, Sect. 5 will be devoted to some conclusions.

## 2 Experimental investigation

Uniaxial compression tests are carried out on disk samples (Fig. 1) obtained by laser-cutting PMMA plates. In order to achieve the release of residual stresses resulting from the machining, the samples are subjected to a heat treatment for 90 min at a temperature of 90 °C, followed by a slow cooling process in the oven. All samples are 8 mm thick to ensure plane strain conditions, following the relationship  $t \geq 2.5 \ell_{ch}$ ,  $\ell_{ch} = (K_{Ic}/\sigma_c)^2$  being the well-known Irwin's length. Its value typically ranges between 0.2 and 1 mm for PMMA (Taylor 2007), (Seweryn 1994). It is worth noting that under uniaxial compression, excluding the contact zones, a tensile stress state is induced along the  $y$ -axis, ( $Oxy$ ) being the Cartesian frame of reference centered on the disk (Fig. 1).

Two configurations are analyzed in the present study: a circular hole with eccentricity  $e$  equal to 0 and 20 mm. For each of them, four different hole radii  $\rho = 0.5, 1, 2$  and 4 mm are considered (Fig. 1). The external radius  $R$  of the disk is fixed and set equal to 40 mm. As highlighted in Fig. 1, the upper and lower parts of the disk are slightly flattened to facilitate the positioning of the sample in the testing machine. This configuration, where two parallel flat ends substitute the curved jaws, is commonly used to guarantee the effectiveness of this test and improve the accuracy of

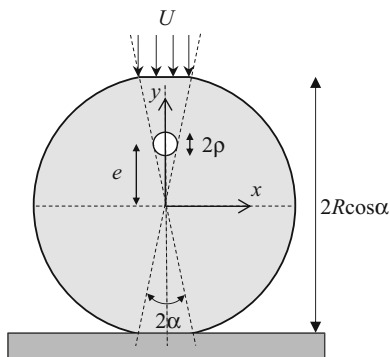


**Fig. 1** Geometry of the Disk specimen containing a hole (diameter  $2\rho$ , eccentricity  $e$ )

the estimation of the tensile strength. Indeed, this loading setup generally guarantees crack initiation at the center of the disk avoiding local cracking in the region close to the contact zone. Uniaxial compression is ensured by having a fixed platen on one side and a spherically seated one on the other, so that possible (small) imperfections in the sample machining for the flat plane have no influence on the prescribed load. (Wang and Xing 1999) introduced the flattened Brazilian disk (BD) test and subsequently, the influence of the loading angles was investigated by (Wang et al. 2004), (Lin et al. 2016) and (Wu et al. 2018). In the present study, the loading angle  $2\alpha$  is set equal to  $20^\circ$ , as typically done in the experimental practice (Wang and Xing 1999; Wu et al. 2018).

The experimental campaign is performed at a constant displacement rate of 1 mm/min by exploiting a Zwick 1455 testing machine. Five samples for each value of eccentricity  $e$  and hole radius  $\rho$  are considered. Samples are coated with black and white sprays to obtain black freckles. In this way, the strain distribution can be monitored during the test using digital image correlation, which is not addressed in the present paper. Some specimens broke in the contact zone with the testing machine. However, at least three values of the failure loads  $P_f$  are obtained for each geometry with failure from the hole, as shown in Table 1. The presence of an eccentric hole decreases the strength if compared to the geometry with a central hole. Specifically, for  $e = 20$  mm,  $\rho = 0.5$  mm and 4 mm, the experimental failure loads are approximately 10% lower than those obtained for  $e = 0$  mm, while this difference decreases to around 2% for radii values of 1 and 2 mm. Moreover, the material behavior is almost linear and the failure is of brittle character, as evident from the force–displacement curves represented in Fig. 2a, b.

One broken sample for each configuration is shown in Fig. 3. As evident from these images, crack propagates along the  $y$ -axis. It is noteworthy that the specimens exhibit stable crack growth before the final unstable crack propagation leading to their failure. Only for ( $\rho = 2$  mm,  $e = 0$  mm) and ( $\rho = 4$  mm,  $e = 0, 20$  mm), the crack propagation always reveals unstable. For the samples showing stable crack growth, initiation loads  $P_c$  are around 2–3% lower than the failure ones  $P_f$ .

Fractographic analyses are conducted to investigate the fracture surfaces of the tested samples. Generally,

**Table 1** Compression tests on PMMA holed samples ( $R = 40$  mm): recorded failure loads and standard deviations

$e$ (mm)	$\rho$ (mm)	$P_f$ (N)					$P_{f, \text{avg}}$ (N)
0	0.5	15,377	15,461	15,080	–	–	$15,306 \pm 163$
	1	12,737	11,070	11,816	–	–	$11,874 \pm 682$
	2	12,238	11,888	9014	9070	–	$10,553 \pm 1516$
	4	9919	10,650	10,404	12,879	11,906	$11,151 \pm 1085$
20	0.5	14,112	14,620	14,723	13,911	13,304	$14,134 \pm 514$
	1	12,817	10,674	11,133	12,577	–	$11,462 \pm 811$
	2	11,220	12,935	9433	8016	10,760	$10,473 \pm 1662$
	4	9873	9753	9668	9868	–	$9791 \pm 86$

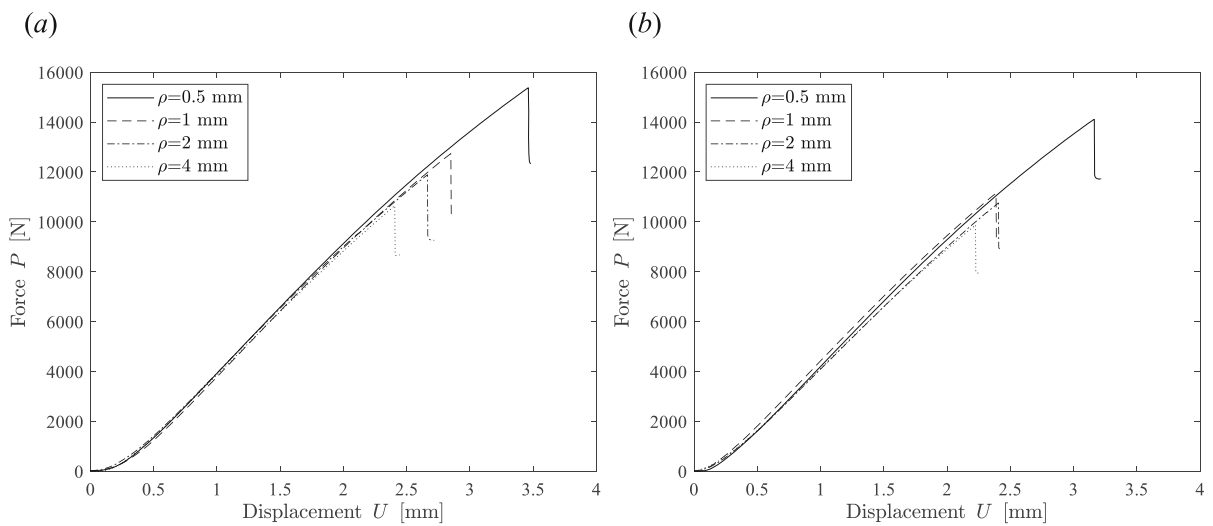
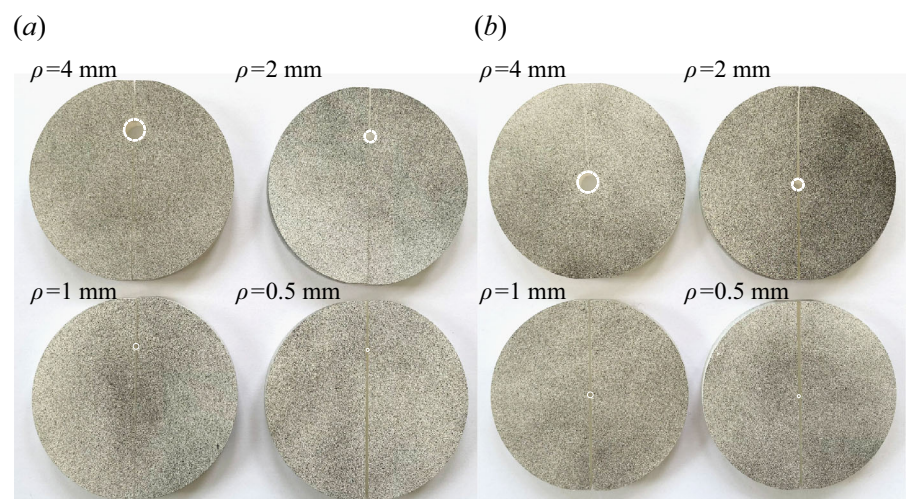


**Fig. 2** Force–displacement curves related to the configuration with **a**  $e = 0$  mm and **b**  $e = 20$  mm. In both figures, for each configuration, only one specimen is presented for the sake of clarity

**Fig. 3** Samples after failure considering four different hole radii  $\rho = 0.5, 1, 2$  and  $4$  mm, presenting a central **a** and eccentric **b** circular hole



two different types of fracture surfaces are observed: (i) a crack propagating through the entire thickness of the sample (see Fig. 4a) or (ii) a small semi-elliptical crack originating from a defect present at the hole edge (see Fig. 4b). In both cases, a mirror-like fracture surface is observed in correspondence to the initiation and propagation up to the end of the stable crack growth, which was checked by comparing the crack extent on the fracture surface to the crack extent on the specimen face measured by the camera. The surface thereafter becomes noticeably rougher, indicating an unstable propagation phase corresponding to specimen failure.

To investigate the crack propagation stability, an ultrahigh-speed acquisition camera Phantom v2012 is employed with a sample rate of 240,000 fps. Thanks to this setup, we were able to track the tip of the crack and thus monitor the crack length during the stable crack growth phase. Images are acquired with a 128 pixels (H)  $\times$  256 pixels (V) resolution and the measurement uncertainty is assessed at  $\pm 1$  pixel, equivalent to approximately  $\pm 0.2$  mm.

Considering the configuration with a central hole, the crack lengths at the end of the stable growth phase are shown in Fig. 5a for two samples with  $\rho = 0.5$ , 1 mm. For these radius values, an asymmetric crack propagation was observed experimentally. Crack

length values are reported in Table 2 where  $a_{1,\text{exp}}$  denotes the experimental length of the crack propagating from the top of the hole whereas  $a_{2,\text{exp}}$  indicates the bottom one.

Analogously, the crack lengths for three geometries with an eccentric hole are depicted in Fig. 5b. These configurations underwent asymmetric crack growth, occurring either from both the top and bottom of the hole or exclusively from the top side.

To complete the experimental analysis, the ultrahigh-speed camera is used also to determine the crack speed during the final unstable crack growth. The average values of the crack speed are reported in Fig. 5c. Considering the geometries with  $e = 0$  mm, the average crack speed ranges between 450 m/s and 550 m/s as  $\rho$  varies. On the other hand, for  $e = 20$  mm, the average crack speed approaches 700 m/s for  $\rho = 0.5$  mm, while it decreases to 500 m/s for all other  $\rho$ . These values are lower than the Rayleigh's speed, which is equal to 860 m/s considering the PMMA properties reported in Table 3.

The mechanical properties of PMMA are reported in Table 3. Young's modulus  $E$  as well as Poisson's ratio  $\nu$  are estimated following ASTM D638-14 standard code. Instead, the ultimate tensile strength  $\sigma_c$  is derived from the bending strength  $\sigma_b$ . Bending tests are particularly useful for brittle materials that

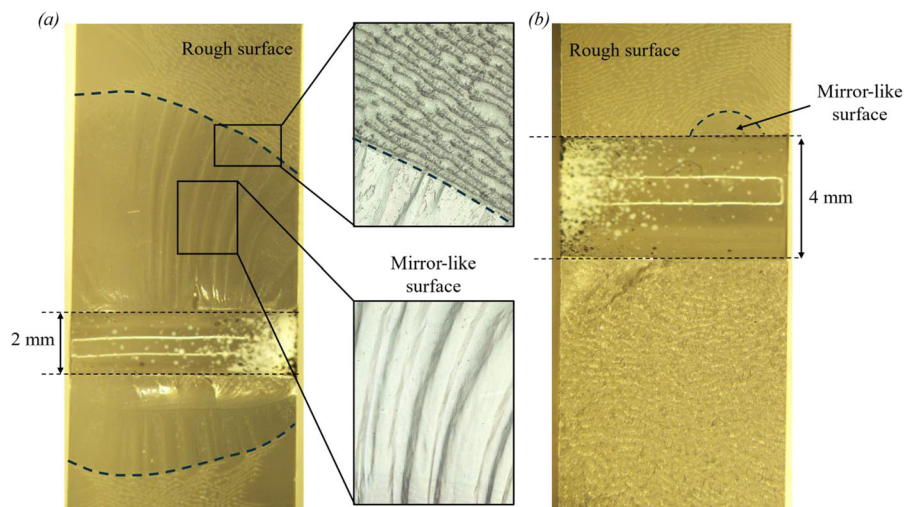


**Fig. 4** Fracture surfaces observed in two tested samples with  $e = 20$  mm: **a** a crack propagating through the entire thickness of the sample, and **b** a small semi-elliptical crack originating from a defect present at the hole edge. The blue line in both

figures represents the boundary between the mirror-like surface and the rougher surface, corresponding to the unstable crack propagation phase

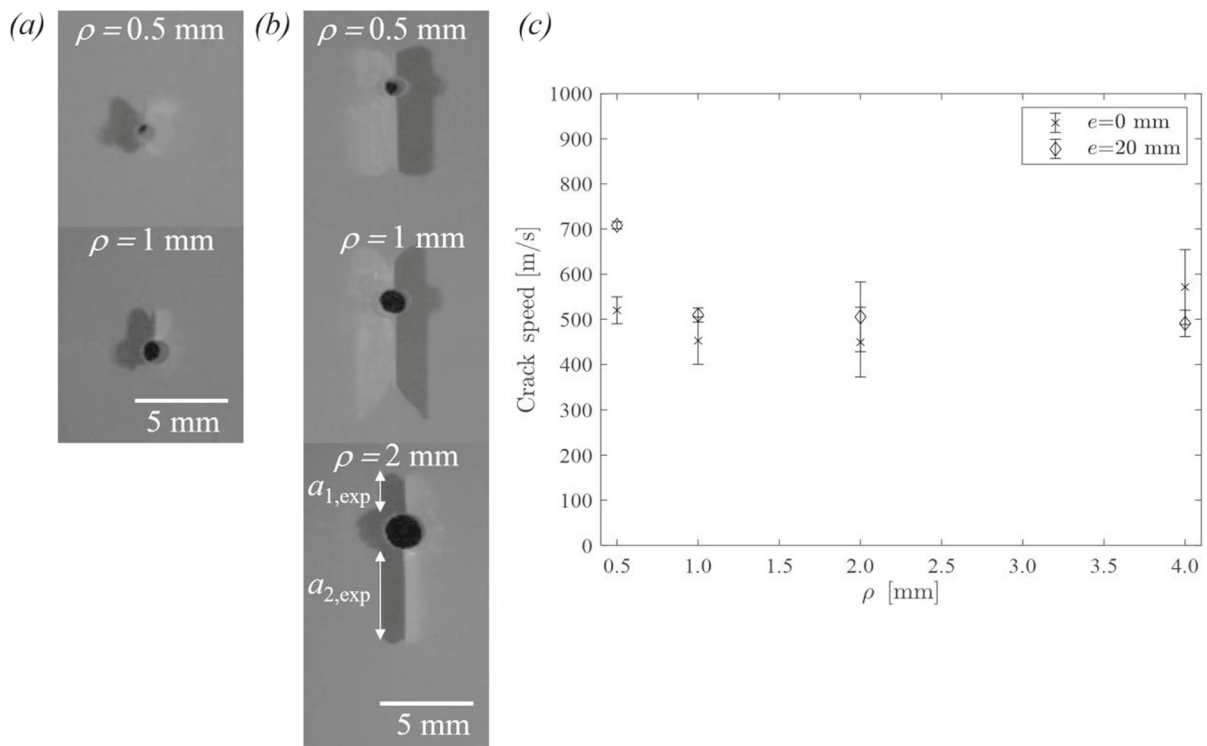


**Fig. 5** Crack lengths at the end of the stable growth phase for the configuration characterized by **a**  $e = 0$  mm and **b**  $e = 20$  mm. **c** Average values of the crack speed during the final unstable propagation

**Table 2** Experimental crack length values at the end of the stable growth phase

$e$ (mm)	$\rho$ (mm)	$a_{1,exp}$ (mm)					$a_{2,exp}$ (mm)				
0	0.5	0	1.4	0	–	–	0.9	0	1.1	–	–
	1	2.4	3.2	0	–	–	0	0	2.8	–	–
20	0.5	1.2	0.6	0	0.9	0	3.5	1.2	0.9	2.0	1.3
	1	1.1	2.1	1.6	0.9	–	0	5.3	4.6	0	–
	2	1.5	3.4	2.1	2.9	2.4	0	0	8.2	8.3	0

might not perform well in tensile tests due to their proneness to premature fracture from a ‘defect’ generated during the machining. Indeed, the stress distribution along the sample during a bending test enables a more controlled failure mode. The bending strength is evaluated through three-point bending tests on three plain specimens with dimensions 74 mm × 8 mm × 20 mm (span × height × width). The tensile strength is determined as  $\sigma_b/1.072$ , extrapolating the correlation factor proposed by (Baldassari et al. 2023), who investigated the size effect on flexural strength of plain specimens as function of the

**Table 3** Measured PMMA mechanical properties, from left to right the material strength, the bending stress at failure, Young’s modulus and Poisson’s ratio

$\sigma_c$ (MPa)	$\sigma_b$ (MPa)	$E$ (GPa)	$\nu$
$67.1 \pm 4.8$	$72.0 \pm 5.1$	$2.69 \pm 0.03$	$0.35 \pm 0.014$

dimensionless structural size  $h/\ell_{ch}$ , where  $h$  is the height of the sample. This value of the correlation factor is valid for sufficiently high  $h/\ell_{ch}$  ratios when the beam slenderness tends to infinity.

### 3 Finite fracture mechanics

#### 3.1 Crack initiation scenarios

For a BD test on a plain circular sample, for a fixed radius, the biaxial stress ratio  $\beta = \sigma_{yy}(y/R)/\sigma_{xx}(y/R)$  varies along the  $y$ -axis. Indeed, the tensile stress  $\sigma_{xx}$  remains approximately constant, while the compressive stress  $\sigma_{yy}$  varies, reaching its minimum  $-3\sigma_{xx}$  at the center of the disk. All in all, we have:

$$\beta(y/R) = -\frac{3 + (y/R)^2}{1 - (y/R)^2} \tag{1}$$

According to Eq. (1), the biaxial stress ratio  $\beta$  is equal to  $-3$  for  $y = 0$  and it decreases moving far from the center (reaching  $-4.3$  for  $y/R = 0.5$ ).

Considering the presence of a circular hole with its center located along the  $y$  axis and with radius small compared to the radius of the disk, the stress concentration factor  $K_t$  can be expressed as  $3 - \beta$ . This value of  $K_t$  can be obtained by considering the (Kirsch 1898) solution for a circular hole in an infinite slab subjected to remote biaxial loading, as presented by (Sapora and Cornetti 2018).

Therefore, we have  $K_t = 6$  for  $e = 0$  mm and  $K_t = 7.3$  for  $e = 20$  mm. It is noteworthy that these values hold true for low  $\rho/R$  ratios. If not, the stress concentration increases and thus a correction factor needs to be considered. Furthermore, considering an eccentric hole located over the  $x$ -axis, the stress concentration on the top of the hole is larger with respect to the bottom side for sufficiently large  $\rho/R$  ratios.

As discussed in the previous section, the configurations investigated in the present study differ from the Brazilian disk geometry since two parallel flat ends are machined. Considering the geometries with a central circular hole, the stress distribution along the loading diameter is almost identical to the BD configuration and  $K_t = 5.8$ . This value increases to 6.2 for  $\rho = 4$  mm due to the finite size effect. Taking into account the geometries with  $e = 20$  mm, the discrepancy in the stress distribution is larger and it increases with the radius. Indeed, the hole is closer to the contact zone and therefore the influence of the flattened ends is higher. For  $\rho = 0.5$  mm,  $K_t$  is equal to 6.7 whereas its value increases for higher  $\rho/R$  ratios up to 8.5 for  $\rho = 4$  mm.

Based on experimental observations and theoretical considerations regarding the stress concentration factors, different crack initiation scenarios are investigated for the analyzed geometries. Considering the configurations characterized by  $e = 0$  mm, a symmetric crack initiation (starting from the hole edge along the  $y$ -axis, see Fig. 6b) should be preferred over an asymmetric one, as more convenient from an energetic point of view (Sapora et al. 2018). In the present study, however, both scenarios will be investigated, for the sake of completeness.

Analogously, taking into account the geometries with an eccentric hole, two distinct scenarios are analyzed: asymmetric crack initiation from the top of the hole edge (Fig. 6a) and asymmetric crack initiation from both the top and the bottom of the hole (Fig. 6c). For each scenario, crack initiation will be evaluated according to the FFM approach.

#### 3.2 Finite fracture mechanics

Following the coupled FFM approaches, stress and energy requirements have to be simultaneously fulfilled for brittle crack initiation to take place. The stress condition, as originally proposed by (Leguillon 2002), states that the normal stress must exceed the ultimate tensile strength  $\sigma_c$  over a finite distance  $\ell$ . The approach can be also developed considering an average stress requirement, as suggested by (Cornetti et al. 2006). Considering the crack initiation scenarios presented in Fig. 6a, b this stress condition leads to the following expression:

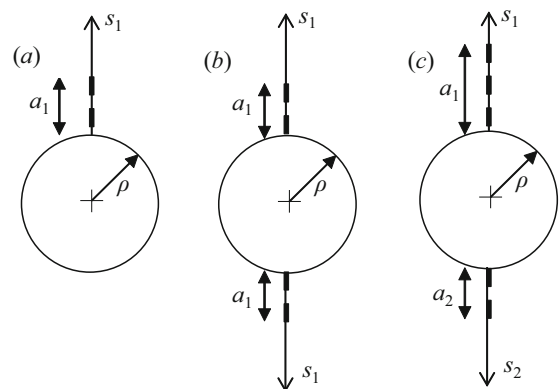


**Fig. 6** Possible scenarios for crack initiation include: asymmetric crack initiation from the top **a** of the hole edge, **b** symmetric crack initiation, and **c** asymmetric crack initiation simultaneously from both the top and bottom of the hole

$$\bar{\sigma}_{xx}(\ell) = \frac{1}{\ell} \int_0^\ell \sigma_{xx}(s_1) ds_1 \geq \sigma_c \tag{2}$$

where  $\sigma_{xx}$  is the tensile stress and  $s_1$  is the coordinate starting from the hole edge along the critical crack path.

Considering the asymmetric crack initiation case (Fig. 6c), condition (2) needs to be satisfied for both the top and bottom crack advances,  $\ell_1$  and  $\ell_2$ , respectively, as proposed by (Rosendahl et al. 2017). The following condition is thus obtained:

$$\bar{\sigma}_{xx}(\ell_i) = \frac{1}{\ell_i} \int_0^{\ell_i} \sigma_{xx}(s_i) ds_i \geq \sigma_c \quad \forall \quad i \in \{1, 2\} \tag{3}$$

On the other hand, the energy balance derives from the energy conservation principle between the states before and after crack nucleation over a finite distance and it involves: the variation of the external work forces ( $\Delta W_{ext}$ ) and of kinetic energy ( $\Delta W_k$ ), elastic strain energy ( $\Delta W_{el}$ ) and crack surface creation energy ( $G_{Ic} \ell$ ). This is expressed as:

$$\Delta W_k + \Delta W_{el} + G_{Ic} \ell = \Delta W_{ext} \tag{4}$$

It is worth mentioning that the energy dissipated through non-linear mechanisms is not considered in Eq. (4).

Considering a displacement controlled test ( $\Delta W_{ext} = 0$ ) under quasi-static loading conditions ( $\Delta W_k \geq 0$ ), Eq. (4) rewrites analogously to Griffith’s criterion  $G \geq G_{Ic}$  (Griffith 1921) in which the ERR  $G$  is replaced by the Incremental Energy Release Rate (IERR)  $G_{inc}$ :

$$G_{inc}(\ell) = \frac{W_{el}(0) - W_{el}(\ell)}{\ell} \geq G_{Ic} \tag{5}$$

Taking into account the asymmetric crack initiation case (Fig. 6c), Eq. (5) needs to be modified to consider the variation of elastic strain energy  $\Delta W_{el}$  related to crack advances  $\ell_1$  and  $\ell_2$ :

$$G_{inc}(\ell_1, \ell_2) = \frac{W_{el}(0, 0) - W_{el}(\ell_1, \ell_2)}{\ell_1 + \ell_2} \geq G_{Ic} \tag{6}$$

Under linear elastic assumptions, the stress is proportional to the prescribed displacement  $U$ , whereas the potential energy is proportional to the square value of  $U$ . Coupling the two conditions above, provided by Eqs. (2) and (5), and considering a

monotonically increasing function  $G_{inc}(\ell)$ , a system of two equations in two unknowns is obtained:

$$\begin{cases} \bar{\sigma}_{xx}(\ell_c, U_c) = k(\ell_c)U_c = \sigma_c \\ G_{inc}(\ell_c, U_c) = A(\ell_c)U_c^2 = G_{Ic} \end{cases} \tag{7}$$

where  $A$  and  $k$  are functions solely dependent on the material properties and specimen geometry. The procedure developed to determine the functions  $k$  and  $A$ , for each analyzed configuration, will be described in Sect. 3.3. The two unknowns of the system i.e., the crack initiation length  $\ell_c$  and the critical applied displacement  $U_c$ , are obtained by solving an implicit equation:

$$\frac{k(\ell_c)^2}{\sigma_c^2} = \frac{A(\ell_c)}{G_{Ic}} \tag{8}$$

On the other hand, considering the asymmetric crack initiation case, coupling Eqs. (3) and (6) yields:

$$\begin{cases} \bar{\sigma}_{xx}(\ell_{ic}, U_c) = k(\ell_{ic})U_c = \sigma_c \quad \forall \quad i \in \{1, 2\} \\ G_{inc}(\ell_{c1}, \ell_{c2}, U_c) = A(\ell_{c1}, \ell_{c2})U_c^2 = G_{Ic} \end{cases} \tag{9}$$

In this case, the unknowns are represented by the critical displacement  $U_c$  and the top and bottom critical crack advances  $\ell_{c1}$  and  $\ell_{c2}$ , respectively. The system (9) is solved numerically considering the minimum value of  $U_c$  satisfying the equations.

### 3.3 Finite element analyses

The functions  $k$  and  $A$ , related to the averaged stress field and IERR, respectively, are here determined through 2D FEAs by ABAQUS® code. Exploiting the symmetry of the structure and of the loading, only half of the geometry is modeled. Linear plane strain elements with 4 nodes are used. To obtain accurate results, following a convergence analysis, the minimum mesh size is set equal to 0.005 mm at the hole edge. The details of the mesh are shown in Fig. 7.

For each analyzed geometry and crack initiation scenario, the stress field and IERR functions along the critical crack path are obtained from  $k$  and  $A$  which are calculated applying a unit displacement. As stated in Sect. 3.1, considering the configurations characterized by a central hole, both asymmetric and symmetric crack initiation are investigated (Fig. 6a, b). The IERR is computed using Eq. (5) by exploiting the ‘unbut-toning’ method: Dirichlet boundary conditions on

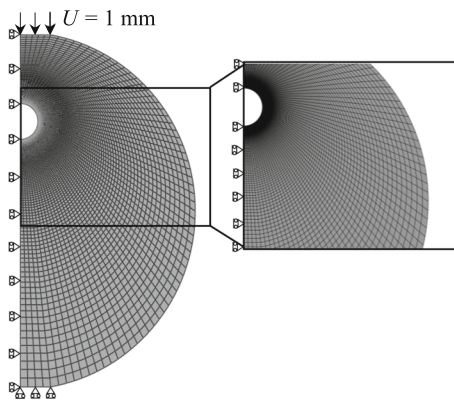


**Fig. 7** Finite element model corresponding to the geometry characterized by  $e = 20$  mm and  $\rho = 4$  mm

nodes along the crack path are successively released allowing the calculation of the elastic strain energy  $W_{el}$  as function of the crack length.

Instead, taking into account the geometries with  $e = 20$  mm, two different scenarios are analyzed: asymmetric single crack initiation from the top (Fig. 6a) and asymmetric double crack initiation either from the top and the bottom of the hole (Fig. 6c). In the latter case, to compute the IERR function  $G_{inc}(a_1, a_2)$  the variation of potential energy  $\Delta W_{el}(a_1, a_2)$  is determined by following the subsequent steps for each geometry:

- Different top crack lengths  $a_1$  are considered ranging between 0 and  $[R \cdot \cos(10^\circ) - (e + \rho)]$  (the top ligament size). For each of these crack lengths, the nodes along the bottom crack path are unbuttoned allowing the calculation of the potential energy  $W_{el}$  as function of bottom crack length. In this way, the blue surface in Fig. 8a is obtained.
- In the same way, different bottom crack lengths  $a_2$  are considered ranging between 0 and  $[R \cdot \cos(10^\circ) + (e - \rho)]$  (the bottom ligament size). For each of these crack lengths, the nodes along the top crack path are unbuttoned allowing the calculation of the elastic strain energy  $W_{el}$  as function of the top crack length. In this way the red surface in Fig. 8a is computed.
- Finally, for each couple of top and bottom crack length values  $(a_1, a_2)$ , the maximum IERR value is considered, thus obtaining the function  $G_{inc}(a_1, a_2)$  plotted in Fig. 8b.

### 3.4 Stability discussion

Considering the central hole configurations, the IERR functions for symmetric and asymmetric crack propagation, obtained by applying a unit displacement as boundary condition, are reported in Fig. 9. Analyzing the symmetric crack initiation scenario, the functions  $G_{inc}(a)$  are monotonically increasing for all considered radii (Figs. 9a, b) thus leading to positive geometries. Therefore, the crack initiation length  $l_c$  and the critical applied displacement  $U_c$ , provided by the FFM approach, are obtained by solving Eq. (8).

Instead, taking into account the asymmetric case, the IERR functions present a local maximum and minimum as  $a$  varies. Thus, following the terminology proposed by (Weißgraeber et al. 2016), (Sapora and Cornetti 2018), these configurations are locally negative and globally positive. In Fig. 9a, considering  $G_{inc}(a)$  for  $\rho = 0.5$  mm,  $a^*$  denotes the crack length corresponding to the local maximum of the function, whereas  $a^{**}$  indicates the other crack length that leads to the same IERR value. Considering the FFM approach, denoting by  $l_s$  the generic solution of system (7), two situations can occur:

1.  $l_s < a^*$  or  $l_s > a^{**}$ : in this case  $l_c = l_s$ , FFM predictions are thus obtained by solving system (7), as previously discussed for a positive configuration.
2.  $a^* < l_s < a^{**}$ : in this case  $l_c = a^*$ , since no crack can develop within the range between  $a^*$  and  $a^{**}$ . In such a case, the stress condition remains fulfilled and the FFM criterion is expressed by imposing  $l_c = a^*$  in the energy balance (4) (Mantič 2009).

Considering the geometries characterized by an eccentric hole, function  $G_{inc}(a)$  related to crack initiation from the top of the hole is reported in Fig. 10. In this case, the geometries are locally positive and globally negative for all the radii values. Thus, as discussed previously, if  $l_s < a^*$  FFM predictions are provided by solving system (7) considering  $l_c = l_s$ , whereas if  $l_s > a^*$  the FFM criterion is expressed by imposing  $l_c = a^*$  in the energy balance (4). Finally, taking into account the crack initiation scenario from both the top and the bottom of the hole,  $G_{inc}(a_1, a_2)$  is depicted in Fig. 8b. In this case the analysis is more complex since the IERR function is represented from a surface and not a curve. Thus, to

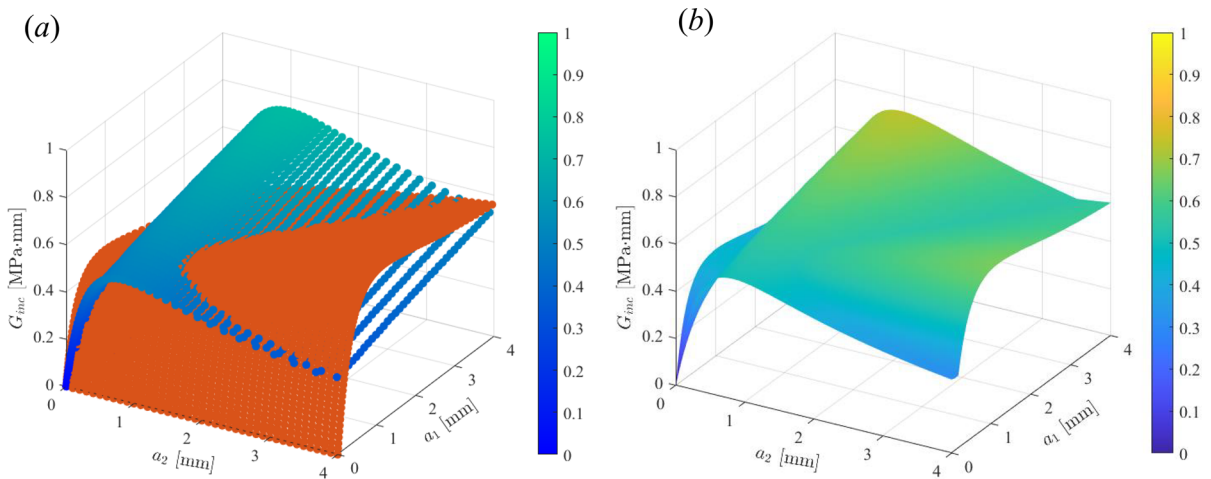


**Fig. 8** Geometry characterized by  $e = 20$  mm and  $\rho = 2$  mm: **a** blue/red IERR function for a fixed bottom/top crack, considering nodes unbuttoning along the top/bottom crack path;

**b**  $G_{inc}(a_1, a_2)$  function obtained taking into account the maximum IERR value for each  $(a_1, a_2)$

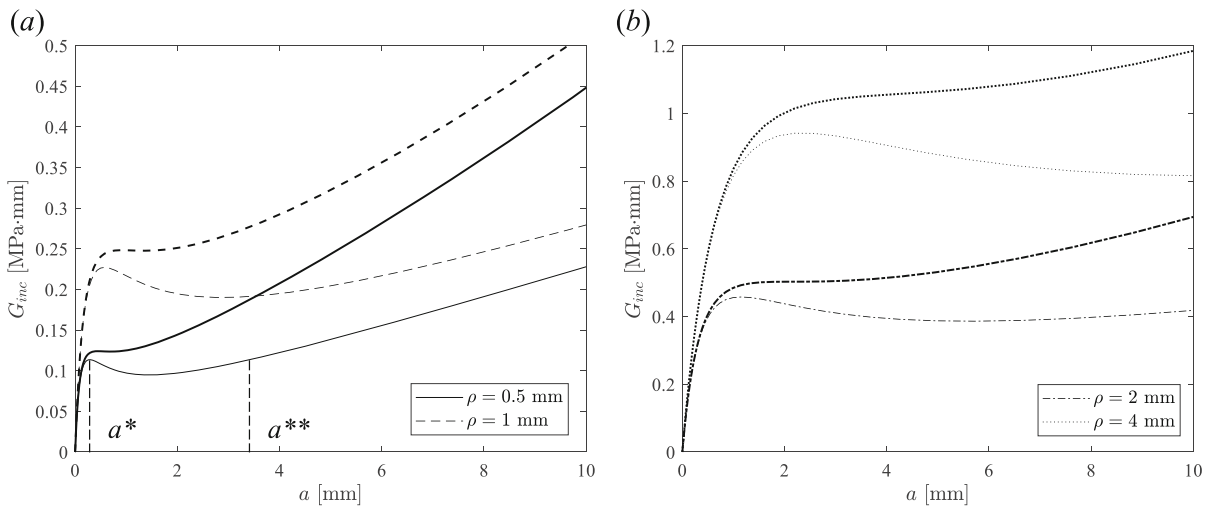


**Fig. 9** IERR functions related to  $e = 0$  mm: **a**  $\rho = 0.5$  mm, 1 mm and **b**  $\rho = 2$  mm, 4 mm. Thick lines refer to the symmetric case, whereas thin lines represent the asymmetric scenario

evaluate the positivity/negative of the configuration, the derivative of  $G_{inc}(a_1, a_2)$  should be evaluated for each couple of top and bottom crack length values  $(a_1, a_2)$ .

Once crack initiation is predicted by FFM, crack propagation stability can be assessed using the concepts of Linear Elastic Fracture Mechanics (LEFM). Considering a globally positive/locally negative configuration, for cracks with length  $a$  up to  $a^*$  or larger than  $a^{**}$ , the incremental release rate is smaller than the differential counterpart, as depicted in Fig. 11. All

nucleated cracks with a length  $a > a^{**}$  are unstable since they are associated with a positive derivative of the differential energy release rate. For a crack with length equal to  $a^*$ , the values of  $G$  and  $G_{inc}$  coincide and the derivate of the former is negative, therefore the crack propagation is stable. Finally, taking into account a finite crack  $a$  shorter than  $a^*$ , unstable crack propagation will take place since  $G > G_{Ic}$ . While growing, the crack can reach a point where the differential energy release rate is lower than the critical energy release rate  $G_{Ic}$ , resulting thus in a

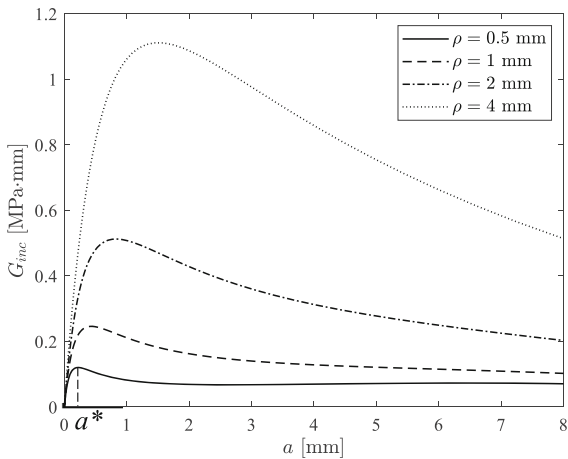


**Fig. 10** IERR functions related to geometries with an eccentric hole considering crack propagation from the top of the hole

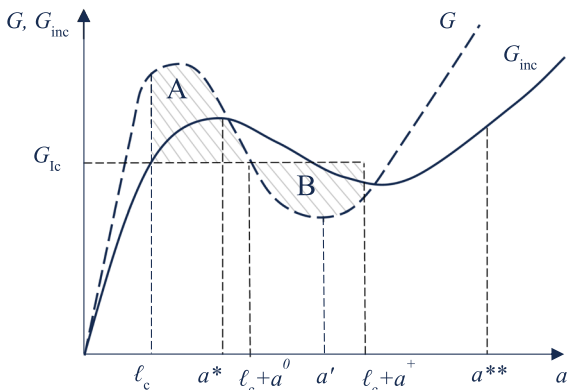


**Fig. 11**  $G$  and  $G_{inc}$  curves related to a globally positive/locally negative configuration

crack arrest. Increasing the loading, the crack will propagate in a stable way up to a length  $a'$ , corresponding to the local minimum of  $G$ , and then, for  $a > a'$ , unstable crack propagation will take place leading to the failure of the sample.

Figure 11 illustrates a possible crack arrest scenario. As stated previously, the crack  $l_c$  propagates at least up to a crack length of  $l_c + a^0$  where the differential energy release rate is equal to the critical one. For longer cracks  $G < G_{Ic}$ , however, since an excess of energy is available during crack propagation up to  $l_c + a^0$  (Area A in Fig. 11), further crack growth can take place. If this excess of energy is available for additional crack propagation  $a^+$  depends on both structural configuration and dynamic fracture effects, as discussed by (Leguillon and Martin 2013). Defining

the fraction of excess energy available for further crack propagation as  $\Omega$ , the maximum crack advancement  $l_c + a^+$  can be assessed by comparing the energy used for crack propagation with the available fraction of excess energy:

$$\Omega \cdot \int_{l_c}^{l_c+a^0} [G(a) - G_{Ic}] da = \int_{l_c+a^0}^{l_c+a^+} [G_{Ic} - G(a)] da \tag{10}$$

where the integral at the left hand side represents area A in Fig. 11, whereas the integral at the right hand side corresponds to area B.

Hence, considering Eq. 10, the excess of energy, whether sufficiently high, can lead to unstable crack propagation, bypassing the region where  $G$  is lower than  $G_{Ic}$  with a negative derivative, and thus the stable crack growth phase.

Crack re-initiation examples resulting from an excess of kinetic energy in dynamic fracture scenarios are presented by (Ravi-Chandar and Knauss 1984), who discussed crack initiation and growth under dynamic loadings. Furthermore, (Chao Correias et al. 2024) developed a comprehensive comparison between quasi-static and dynamic approaches regarding multi-ligament fracture conditions, showing the limitations of the quasi-static hypothesis.

## 4 Predictions versus experimental results

### 4.1 Crack initiation

FFM predictions are now compared with the experimental data presented in Sect. 2. To implement the FFM approach, the critical value of the Energy Release Rate  $G_{Ic}$  is first evaluated by minimizing the standard deviation between the experimental data and FFM failure estimations related to the configurations presenting a central hole ( $e = 0$  mm). Accordingly,  $G_{Ic}$  is estimated equal to 0.16 MPa·mm (160 J/m<sup>2</sup>). This value will be implemented later on in this section for blind predictions on samples related to  $e = 20$  mm.

It is worth mentioning that the above value for  $G_{Ic}$ , considering Young's modulus and Poisson's ratio reported in Table 3, corresponds to a critical stress intensity factor  $K_{Ic} = \sqrt{(G_{Ic} \cdot E / (1 - \nu^2))} = 0.7$  MPa√m. Exploring the scientific literature, (Berto et al. 2013) and (Cicero et al. 2018) obtained a value of

$K_{Ic} = 2.04 \text{ MPa}\sqrt{\text{m}}$  testing Single edge Notch Bending (SENB) specimens containing U-shaped notches. Similarly, (Taylor 2007) and (Sapora et al. 2023) observed high values of the fracture toughness equal to  $2.23 \text{ MPa}\sqrt{\text{m}}$  and  $2.15 \text{ MPa}\sqrt{\text{m}}$  respectively. (Seweryn et al. 1997) and (Seweryn and Łukaszewicz 2002), considering V-notched samples, respectively found  $K_{Ic} = 1.37 \text{ MPa}\sqrt{\text{m}}$  and  $K_{Ic} = 1.202 \text{ MPa}\sqrt{\text{m}}$ . Additionally, similar values of the fracture toughness ranging between 1.3 and  $2 \text{ MPa}\sqrt{\text{m}}$  were observed also by (Sapora et al. 2018), (Torabi et al. 2017), (Leite et al. 2021) and (Seldén 1987) who tested compact tension specimen. Lower values were obtained by (Dunn et al. 1997), who determined  $K_{Ic} = 1.02 \text{ MPa}\sqrt{\text{m}}$  using SENB specimens with an initial crack machined with a sharp razor blade, and by (Choi and Salem 1993) that obtained an average value of the fracture toughness equal to  $1.08 \text{ MPa}\sqrt{\text{m}}$  exploiting an indent strength method. Analogously, a value of  $K_{Ic} \cong 1.0 \text{ MPa}\sqrt{\text{m}}$  for PMMA was obtained also by (Li and Zhang 2006) and (Zhang et al. 2014). Furthermore, low values of the fracture toughness ranging between  $0.54 \text{ MPa}\sqrt{\text{m}}$  and  $0.92 \text{ MPa}\sqrt{\text{m}}$  were obtained by minimizing the deviation between FFM predictions and experimental results for different geometries and loading conditions (Doitrand et al. 2019; Doitrand et al. 2021a, b; Duminy et al. 2024).

Based on these observations and considering the typical fracture toughness values  $0.7 \text{ MPa}\sqrt{\text{m}} \leq K_{Ic} \leq 1.6 \text{ MPa}\sqrt{\text{m}}$  indicated for PMMA by (Lampman 2003), it can be stated that the value implemented in this study,  $K_{Ic} = 0.7 \text{ MPa}\sqrt{\text{m}}$ , falls within the typical range measured for PMMA.

For all analyzed configurations, considering the material properties  $\sigma_c$  and  $G_{Ic}$ , the solution of system (7)  $\ell_s$  results in values lower than  $a^*$ . Thus, based on the considerations developed in Sect. 3.4, we have  $\ell_c = \ell_s$  and the FFM criterion is actually expressed by systems (7) and (9).

Taking into account the samples with a central hole ( $e = 0 \text{ mm}$ ), strength estimations according to FFM considering symmetric crack initiation are compared with the experimental results in Fig. 12a. Strength predictions related to the asymmetric scenario are very close to those referring to the symmetric one, being almost 1% higher.

The deviation of FFM predictions from the average value of the experimental initiation loads is approximately 14% and 11% for the configurations with

$\rho = 2$  and 1 mm, decreasing to 5% and 2.5% for the geometries with  $\rho = 0.5$  and 4 mm, respectively.

Furthermore, the critical crack advance provided by Eq. (7)  $\ell_c$  keeps approximately constant and equal to 0.06 mm, which corresponds to a ratio  $\ell_c/\ell_{ch} \approx 0.55$ . These values are consistent with the results obtained by (Sapora and Cornetti 2018) for a circular hole subjected to biaxial loading. Indeed, for this configuration considering a ratio  $\rho/\ell_{ch} > 1$ , the normalized crack advancement  $\ell_c/\ell_{ch} \rightarrow 2/(\pi 1.12^2) \approx 0.51$ .

Considering the geometries characterized by  $e = 20 \text{ mm}$ , the comparison between the strength estimations provided by FFM and experimental results is presented in Fig. 12b. Two different crack initiation scenarios are analyzed: (i) asymmetric crack initiation from the top of the hole (Fig. 6a) and (ii) simultaneous initiation from both the top and the bottom of the hole (Fig. 6c). The most critical one results to be the crack initiation from the top of the hole, although the difference for low radii is not noticeable (less than 1%).

As shown in Fig. 12b FFM predictions are again in agreement with the experimental results. Indeed, considering the most critical scenario, the deviation from the average value of  $P_c$  is around 7% for  $\rho = 4 \text{ mm}$  and decreases to nearly 2% for other configurations. Finally, the critical crack advances  $\ell_c$  keeps approximately constant and equal to 0.06 mm for the top initiation (Fig. 6a). Instead, considering the crack initiation scenario reported in Fig. 6c,  $\ell_{c1}$  and  $\ell_{c2}$  are equal to  $\approx 0.06 \text{ mm}$  and  $0.052 \text{ mm}$  for  $\rho = 0.5 \text{ mm}$ , respectively. As the radius increases, the critical crack advance values decrease and finally increase up to  $\ell_{c1} \approx 0.077 \text{ mm}$  and  $\ell_{c2} \approx 0.013 \text{ mm}$  for  $\rho = 4 \text{ mm}$ .

## 4.2 Crack growth

Once crack initiation is predicted by FFM, crack growth stability can be assessed by exploiting the concepts of LEFM, and thus analyzing the differential energy release rate  $G$ . Based on quasi-static assumption, the critical value  $G_{Ic}$  is considered as a constant value.

As discussed in the previous section, for all analyzed configurations, considering different crack initiation scenarios, the solution of the system (7)  $\ell_s$  results lower than  $a^*$ , and thus  $\ell_c = \ell_s$ . Thus, based on

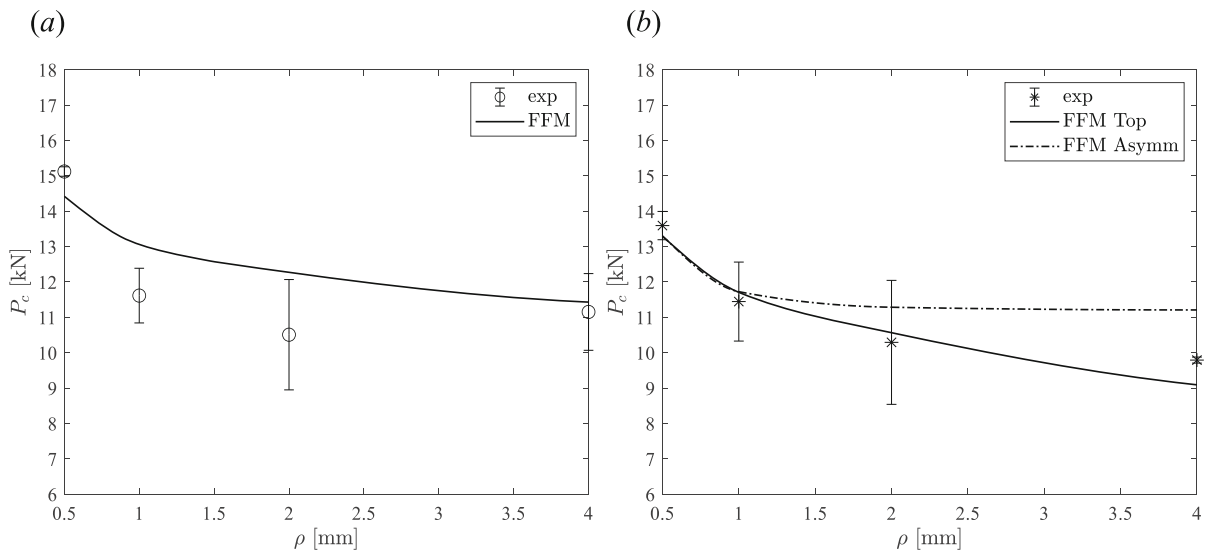


**Fig. 12** FFM predictions versus experimental initiation loads for  $e = 0$  mm **a** and  $e = 20$  mm **b**

the considerations developed in Sect. 3.4, for a globally positive/locally negative configuration (Fig. 11), the crack propagates from a crack length  $\ell_c$  up to at least a crack length of  $\ell_c + a^0$  where the differential energy release rate is equal to the critical one. Then, a stable crack growth phase can occur increasing the external load up to a length  $a'$ , corresponding to the local minimum of  $G$ . Finally, an unstable crack growth takes place for  $a > a'$  leading to the failure of the sample.

Focusing on the centrally holed geometries, asymmetric crack propagation is observed for all tested samples. Considering this crack initiation scenario, the configurations are globally positive/locally negative, and thus the previous considerations hold true.

With the experimental setup presented in Sect. 2, we are not able to capture and record the initial unstable crack initiation phase and thus only the stable growth is investigated experimentally. In particular, the crack lengths at the end of the stable crack growth, reported in Table 2, are compared with the values of  $a'$ . In Fig. 13a, the  $G$  and  $G_{inc}$  functions for the three tested samples with  $\rho = 0.5$  mm are reported. These curves correspond to an applied load  $P_f$ , since this is the loading condition at the end of the stable crack growth phase. For this geometry, the crack length  $a' = 0.84$  mm is nearly 25% lower than the average experimental crack length. Similarly, considering the configuration with  $\rho = 1$  mm, the

discrepancy between  $a' = 1.7$  mm and the average experimental value is almost 40%. These discrepancies between the values of  $a'$  with respect to the experimental crack lengths at the end of the stable crack growth phase can be explained by considering the 'excess energy' available during crack propagation for further crack growth (Fig. 14).

Furthermore, in this analysis, it is worth noting that samples with  $\rho = 2$  mm and 4 mm did not show a stable crack propagation phase. This behavior might be explained once again by considering that the unstable crack growth phase led directly to the failure of the samples due to a sufficiently high 'excess energy', without showing thus the stable crack growth phase.

The same analysis is developed for geometries with  $e = 20$  mm. In this case, in addition to the geometries with radii values equal to 0.5 mm and 1 mm, specimens with  $\rho = 2$  mm also showed a stable crack propagation phase. In particular, samples showed an asymmetric crack growth from both the top and the bottom of the hole or only from the top side. Then, after the stable phase, an unstable crack propagation occurred always from the bottom crack or the bottom of the hole edge. For this reason, the function  $G(a_1, a_2)$  related to bottom crack propagation, was investigated for each sample. This function is obtained considering different values of the top crack  $a_1$  as presented in Sect. 3.4. In this analysis, the experimental bottom

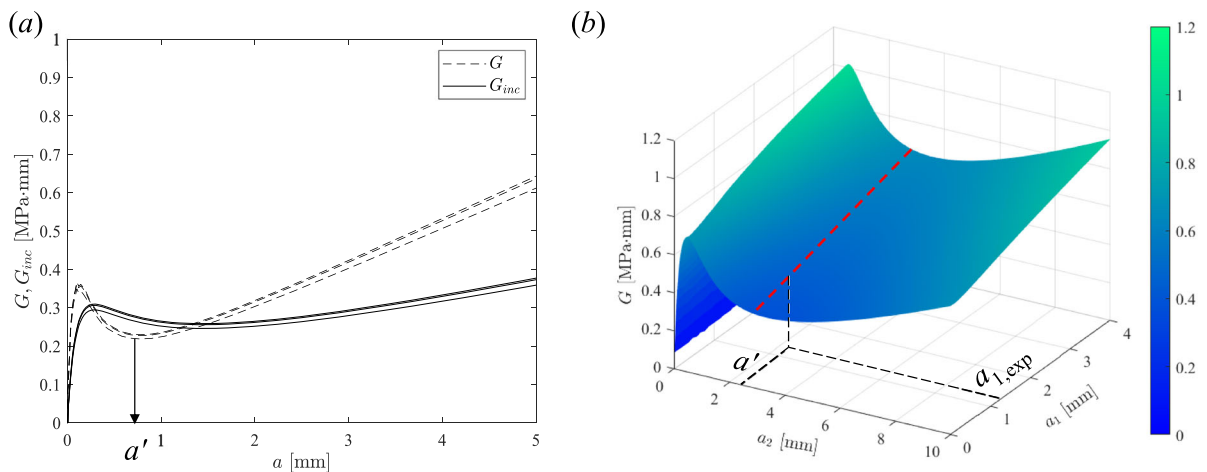


**Fig. 13** **a**  $G_{inc}$  and  $G$  functions at failure for samples with  $\rho = 0.5$  mm and  $e = 0$  mm. **b**  $G(a_1, a_2)$  for propagation from the bottom crack, related to a sample with  $e = 20$  mm and  $\rho = 2$  mm

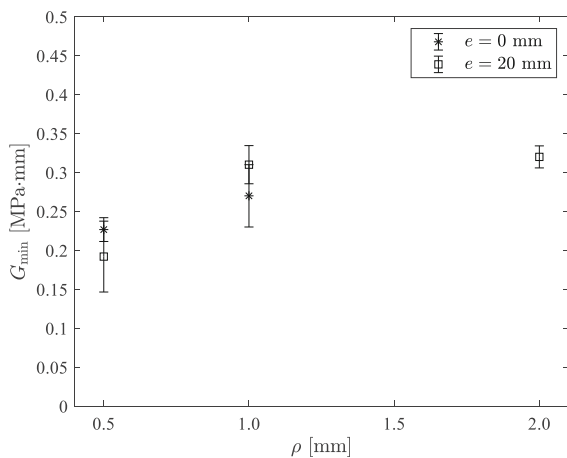


**Fig. 14**  $G_{min}$  values as  $\rho$  varies for all tested samples

crack length at the end of the stable growth phase is compared with  $a'$ , corresponding to the minimum of  $G(a_1, a_2)$  considering a top crack length  $a_1 = a_{1,exp}$ , measured experimentally (Fig. 13b). Considering  $\rho = 0.5$  mm,  $a'$  is ranging between 0.96 mm and 1.13 mm whereas for  $\rho = 1$  mm  $a'$  is almost constant and equal to 2 mm. For  $\rho = 2$  mm  $a'$  is ranging between 3.2 mm and 3.6 mm. Analogously to that stated for the centrally holed geometries, these values of  $a'$  are higher than the experimental crack lengths at the end of the stable phase. Furthermore, it is noteworthy that some samples with  $\rho = 1$  mm and 2 mm (characterized by the highest values of the failure loads), as highlighted in Table 2, and all the specimens with  $\rho = 4$  mm did not show a stable crack

propagation phase from the bottom of the hole. In these cases, unstable crack growth occurred directly from the bottom of the hole edge. As discussed before, these results can be attributed to the excess of energy present during crack propagation.

To conclude this analysis, for the samples that showed a stable crack growth phase, we evaluated the values of  $G_{min}$ , corresponding to a crack length  $a'$ , determined for each sample as previously described. As  $\rho$  varies, the average value of  $G_{min}$  ranges between 0.15 and 0.34 MPa-mm. These higher values with respect to  $G_{Ic}$ , used to implement the FFM approach, might be due to dynamic effects that could characterize the crack initiation phase. In such case, the crack velocity during initiation can be estimated based on the relation between dynamic and quasi-static ERR for a semi-infinite crack in an infinite medium (Freund 1998):

$$G^{dyn} \approx \left(1 - \frac{v_{crack}}{v_{Rayleigh}}\right) G_{QS} \tag{11}$$

where  $v_{crack}$  is the crack velocity and  $v_{Rayleigh}$  the Rayleigh's velocity (Fig. 14).

From this relation and assuming that the crack propagates when  $G^{dyn} = G_{Ic}$ , it yields crack velocities between 170 and 450 m/s for  $G_{min}$  values between 0.15 and 0.34 MPa-mm. These crack velocities are in the order of magnitude, yet smaller than the crack velocities measured during the unstable crack propagation phase. This could be due to relation (11) that may be different from Freund's solution in the case of

a crack initiating and propagating from a hole (Doitrand et al. 2022), (Chen et al. 2023).

## 5 Conclusions

In this work, the failure behavior of eccentric circular holes in PMMA disks under compression load was investigated experimentally. Furthermore, to investigate the failure size effect, four different hole radii were considered.

Experimental results were interpreted in terms of FFM. The coupled approach was implemented numerically, considering different crack initiation scenarios. The most critical one resulted the symmetric crack initiation case for the centrally holed geometries and the asymmetric one (from the top of the edge) for configurations characterized by an eccentric hole. Indeed, the more the hole is eccentric, the less is the strength of the sample. Crack initiation predictions, obtained by implementing numerically the FFM approach, were in agreement with experimental results.

Moreover, the stability of crack growth was discussed for locally negative/globally positive and locally positive/globally negative configurations, using the concepts of LEFM. Finally, exploiting an ultrahigh-speed acquisition camera, the stable crack growth phase was investigated. In particular, the experimental crack lengths at the end of the stable growth were compared with theoretical predictions. Discrepancies were interpreted considering an excess of energy during crack propagation available for further crack advancement. In light of these results, future research directions could include dynamics analyses to evaluate better the influence of dynamic effects on the crack initiation and alternation of stable/unstable crack growth. Moreover, analyses exploiting a different setup could be developed to catch experimentally the unstable crack initiation. This could also help to furnish a deeper physical meaning to the critical crack advancement provided by the FFM approach.

**Author contributions** F. F. wrote the main manuscript text, prepared figures, developed numerical analyses and performed experimental tests. R. E. super.

**Funding** Open access funding provided by Politecnico di Torino within the CRUI-CARE Agreement.

**Data availability** No datasets were generated or analysed during the current study.

## Declarations

**Conflict of interest** The authors declare no conflict of interest.

**Open Access** This article is licensed under a Creative Commons Attribution 4.0 International License, which permits use, sharing, adaptation, distribution and reproduction in any medium or format, as long as you give appropriate credit to the original author(s) and the source, provide a link to the Creative Commons licence, and indicate if changes were made. The images or other third party material in this article are included in the article's Creative Commons licence, unless indicated otherwise in a credit line to the material. If material is not included in the article's Creative Commons licence and your intended use is not permitted by statutory regulation or exceeds the permitted use, you will need to obtain permission directly from the copyright holder. To view a copy of this licence, visit <http://creativecommons.org/licenses/by/4.0/>.

## References

- Awerbuch J, Madhukar MS (1985) Notched strength of composite laminates: predictions and experiments—a review. *J Reinf Plast Compos* 4:3–159. <https://doi.org/10.1177/073168448500400102>
- Baldassari M, Monaco A, Sapora A, Cornetti P (2023) Size effect on flexural strength of notched and un-notched concrete and rock specimens by finite fracture mechanics. *Theor Appl Fract Mech* 125:103787. <https://doi.org/10.1016/j.tafmec.2023.103787>
- Berto F, Campagnolo A, Elices M, Lazzarin P (2013) A synthesis of polymethylmethacrylate data from U-notched specimens and V-notches with end holes by means of local energy. *Mater Des* 49:826–833. <https://doi.org/10.1016/j.matdes.2013.01.074>
- Carrère N, Doitrand A, Martin E, Leguillon D (2021) Theoretical study based on 2D assumptions of the influence of small pores on crack initiation in adhesively bonded joints. *Int J Adhes Adhes* 111:102979. <https://doi.org/10.1016/j.jadhadh.2021.102979>
- Chao Correas A, Sapora A, Reinoso J et al (2023) Coupled versus energetic nonlocal failure criteria: a case study on the crack onset from circular holes under biaxial loadings. *Eur J Mech A/Solids* 101:105037. <https://doi.org/10.1016/j.euromechsol.2023.105037>
- Chao Correas A, Reinoso J, Cornetti P, Corrado M (2024) On the (lack of) representativeness of quasi-static variational fracture models for unstable crack propagation. *J Mech Phys Solids* 186:105573. <https://doi.org/10.1016/j.jmps.2024.105573>
- Chen X, Doitrand A, Godin N, Fusco C (2023) Crack initiation in PMMA plates with circular holes considering kinetic

- energy and nonlinear elastic material behavior. *Theor Appl Fract Mech* 124:103783. <https://doi.org/10.1016/j.tafmec.2023.103783>
- Choi SR, Salem JA (1993) Fracture toughness of PMMA as measured with indentation cracks. *J Mater Res* 8:3210–3217. <https://doi.org/10.1557/JMR.1993.3210>
- Cicero S, Madrazo V, Carrascal IA (2012) Analysis of notch effect in PMMA using the theory of critical distances. *Eng Fract Mech* 86:56–72. <https://doi.org/10.1016/j.engfracmech.2012.02.015>
- Cicero S, Torabi AR, Madrazo V, Azizi P (2018) Prediction of fracture loads in PMMA U-notched specimens using the equivalent material concept and the theory of critical distances combined criterion. *Fatigue Fract Eng Mater Struct* 41:688–699. <https://doi.org/10.1111/ffe.12728>
- Cornetti P, Pugno N, Carpinteri A, Taylor D (2006) Finite fracture mechanics: a coupled stress and energy failure criterion. *Eng Fract Mech* 73:2021–2033. <https://doi.org/10.1016/j.engfracmech.2006.03.010>
- Doitrand A, Estevez R, Leguillon D (2019) Experimental characterization and numerical modeling of crack initiation in rhombus hole PMMA specimens under compression. *Eur J Mech A/Solids* 76:290–299. <https://doi.org/10.1016/j.euromechsol.2019.04.013>
- Doitrand A, Sapora A (2020) Nonlinear implementation of finite fracture mechanics: a case study on notched Brazilian disk samples. *Int J Non Linear Mech* 119:103245. <https://doi.org/10.1016/j.ijnonlinmec.2019.103245>
- Doitrand A, Leguillon D (2021) Asymptotic analysis of pore crack initiation near a free edge. *Theor Appl Fract Mech* 116:103125. <https://doi.org/10.1016/j.tafmec.2021.103125>
- Doitrand A, Cornetti P, Sapora A, Estevez R (2021a) Experimental and theoretical characterization of mixed mode brittle failure from square holes. *Int J Fract* 228:33–43. <https://doi.org/10.1007/s10704-020-00512-9>
- Doitrand A, Henry R, Lube T, Meille S (2021b) Size effect assessment by weibull's approach and the coupled criterion. *Eng Fract Mech* 256:107979. <https://doi.org/10.1016/j.engfracmech.2021.107979>
- Doitrand A, Molnár G, Leguillon D et al (2022) Dynamic crack initiation assessment with the coupled criterion. *Eur J Mech A/Solids* 93:104483. <https://doi.org/10.1016/j.euromechsol.2021.104483>
- Duminy T, Doitrand A, Meille S (2024) Fracture parameter identification by digital image correlation and finite fracture mechanics for millimeter-scale samples. *Eng Fract Mech* 295:109770. <https://doi.org/10.1016/j.engfracmech.2023.109770>
- Dunn ML, Suwito W, Cunningham S (1997) Fracture initiation at sharp notches: correlation using critical stress intensities. *Int J Solids Struct* 34:3873–3883. [https://doi.org/10.1016/S0020-7683\(96\)00236-3](https://doi.org/10.1016/S0020-7683(96)00236-3)
- Felger J, Stein N, Becker W (2017) Mixed-mode fracture in open-hole composite plates of finite-width: an asymptotic coupled stress and energy approach. *Int J Solids Struct* 122–123:14–24. <https://doi.org/10.1016/j.ijsolstr.2017.05.039>
- Freund LB (1998) *Dynamic fracture mechanics*. Cambridge University Press, Cambridge
- Griffith AA (1921) VI. The phenomena of rupture and flow in solids. *Philos Trans R Soc London Ser A Contain Pap a Math or Phys Character* 221:163–198. <https://doi.org/10.1098/rsta.1921.0006>
- Hashin Z (1996) Finite thermoelastic fracture criterion with application to laminate cracking analysis. *J Mech Phys Solids* 44:1129–1145. [https://doi.org/10.1016/0022-5096\(95\)00080-1](https://doi.org/10.1016/0022-5096(95)00080-1)
- Kim S-R, Nairn JA (2000) Fracture mechanics analysis of coating/substrate systems. *Eng Fract Mech* 65:573–593. [https://doi.org/10.1016/S0013-7944\(99\)00141-1](https://doi.org/10.1016/S0013-7944(99)00141-1)
- Kirsch G (1898) *Die Theorie der elastizität und die bedürfnisse der festigkeitslehre*. Zantrolblatt Verlin Deutscher Ingenieure
- Kurguzov V, Kuznetsov D (2024) Fracture analysis of Brazilian circular hole disk under mixed mode loading. *Eng Fract Mech* 297:109875. <https://doi.org/10.1016/j.engfracmech.2024.109875>
- Lampman S (2003) *Characterization and failure analysis of plastics*. ASM International, Materials Park, OH
- Leguillon D (2002) Strength or toughness? A criterion for crack onset at a notch. *Eur J Mech A/Solids* 21:61–72. [https://doi.org/10.1016/S0997-7538\(01\)01184-6](https://doi.org/10.1016/S0997-7538(01)01184-6)
- Leguillon D, Martin E (2013) The strengthening effect caused by an elastic contrast—part I: the bimaterial case. *Int J Fract* 179:157–167. <https://doi.org/10.1007/s10704-012-9787-y>
- Leite A, Mantič V, Paris F (2021) Crack onset in stretched open hole PMMA plates considering linear and non-linear elastic behaviours. *Theor Appl Fract Mech* 114:102931. <https://doi.org/10.1016/j.tafmec.2021.102931>
- Li J, Zhang XB (2006) A criterion study for non-singular stress concentrations in brittle or quasi-brittle materials. *Eng Fract Mech* 73:505–523. <https://doi.org/10.1016/j.engfracmech.2005.09.001>
- Lin H, Xiong W, Yan Q (2016) Modified formula for the tensile strength as obtained by the flattened brazilian disk test. *Rock Mech Rock Eng* 49:1579–1586. <https://doi.org/10.1007/s00603-015-0785-z>
- Mantič V (2009) Interface crack onset at a circular cylindrical inclusion under a remote transverse tension. Application of a coupled stress and energy criterion. *Int J Solids Struct* 46:1287–1304. <https://doi.org/10.1016/j.ijsolstr.2008.10.036>
- Marsavina L, Sapora A, Susmel L, Taylor D (2023) The application of the theory of critical distances to nonhomogeneous materials. *Fatigue Fract Eng Mater Struct* 46:1314–1329. <https://doi.org/10.1111/ffe.13922>
- Neuber H (1936) Theorie der technischen formzahl. *Forsch Auf Dem Gebiete Des Ingenieurwesens* 7:271–274. <https://doi.org/10.1007/BF02584908>
- Peterson RE (1938) Methods of correlating data from fatigue tests of stress concentration specimens. In: Macmillan (ed) *Stephen Timoshenko Anniversary Volume*. New York, pp. 179
- Pipes RB, Wetherhold RC, Gillespie JW (1979) Notched strength of composite materials. *J Compos Mater* 13:148–160. <https://doi.org/10.1177/002199837901300206>
- Ravi-Chandar K, Knauss WG (1984) An experimental investigation into dynamic fracture: I. Crack initiation and arrest. *Int J Fract* 25:247–262. <https://doi.org/10.1007/BF00963460>

- Rosendahl PL, Weißgraeber P, Stein N, Becker W (2017) Asymmetric crack onset at open-holes under tensile and in-plane bending loading. *Int J Solids Struct* 113–114:10–23. <https://doi.org/10.1016/j.ijsolstr.2016.09.011>
- Sakha M, Nejati M, Driesner T (2023) On the initiation of hydraulic fractures in anisotropic rocks. *Int J Rock Mech Min Sci* 169:105429. <https://doi.org/10.1016/j.ijrmmms.2023.105429>
- Sapora A, Cornetti P (2018) Crack onset and propagation stability from a circular hole under biaxial loading. *Int J Fract* 214:97–104. <https://doi.org/10.1007/s10704-018-0315-6>
- Sapora A, Torabi AR, Etesam S, Cornetti P (2018) Finite fracture mechanics crack initiation from a circular hole. *Fatigue Fract Eng Mater Struct* 41:1627–1636. <https://doi.org/10.1111/ffe.12801>
- Sapora A, Ferriani F, Cornetti P et al (2023) Ligament size effect in largely cracked tensile structures. *Theor Appl Fract Mech* 125:103871. <https://doi.org/10.1016/j.tafmec.2023.103871>
- Seldén R (1987) Fracture energy measurements in polycarbonate and PMMA. *Polym Test* 7:209–222. [https://doi.org/10.1016/0142-9418\(87\)90032-8](https://doi.org/10.1016/0142-9418(87)90032-8)
- Seweryn A (1994) Brittle fracture criterion for structures with sharp notches. *Eng Fract Mech* 47:673–681. [https://doi.org/10.1016/0013-7944\(94\)90158-9](https://doi.org/10.1016/0013-7944(94)90158-9)
- Seweryn A, Si P, Mróz Z (1997) Brittle fracture in plane elements with sharp notches under mixed-mode loading. *J Eng Mech* 123:535–543. [https://doi.org/10.1061/\(ASCE\)0733-9399\(1997\)123:6\(535\)](https://doi.org/10.1061/(ASCE)0733-9399(1997)123:6(535))
- Seweryn A, Łukaszewicz A (2002) Verification of brittle fracture criteria for elements with V-shaped notches. *Eng Fract Mech* 69:1487–1510. [https://doi.org/10.1016/S0013-7944\(01\)00138-2](https://doi.org/10.1016/S0013-7944(01)00138-2)
- Tan SC (1987) Fracture strength of composite laminates with an elliptical opening. *Compos Sci Technol* 29:133–152. [https://doi.org/10.1016/0266-3538\(87\)90053-4](https://doi.org/10.1016/0266-3538(87)90053-4)
- Taylor D (2004) Predicting the fracture strength of ceramic materials using the theory of critical distances. *Eng Fract Mech* 71:2407–2416. <https://doi.org/10.1016/j.engfracmech.2004.01.002>
- Taylor D (2006) The theory of critical distances applied to the prediction of brittle fracture in metallic materials. *Struct Durab Heal Monit* 1:145–154. <https://doi.org/10.3970/sdhm.2005.001.145>
- Taylor D (2007) *The theory of critical distances*. Elsevier, London
- Torabi AR, Etesam S, Sapora A, Cornetti P (2017) Size effects on brittle fracture of Brazilian disk samples containing a circular hole. *Eng Fract Mech* 186:496–503. <https://doi.org/10.1016/j.engfracmech.2017.11.008>
- Vedernikova A, Kostina A, Plekhov O, Bragov A (2019) On the use of the critical distance concept to estimate tensile strength of notched components under dynamic loading and physical explanation theory. *Theor Appl Fract Mech* 103:102280. <https://doi.org/10.1016/j.tafmec.2019.102280>
- Wang Q-Z, Xing L (1999) Determination of fracture toughness KIC by using the flattened Brazilian disk specimen for rocks. *Eng Fract Mech* 64:193–201. [https://doi.org/10.1016/S0013-7944\(99\)00065-X](https://doi.org/10.1016/S0013-7944(99)00065-X)
- Wang Q, Jia X, Kou S et al (2004) The flattened Brazilian disc specimen used for testing elastic modulus, tensile strength and fracture toughness of brittle rocks: analytical and numerical results. *Int J Rock Mech Min Sci* 41:245–253. [https://doi.org/10.1016/S1365-1609\(03\)00093-5](https://doi.org/10.1016/S1365-1609(03)00093-5)
- Weißgraeber P, Hell S, Becker W (2016) Crack nucleation in negative geometries. *Eng Fract Mech* 168:93–104. <https://doi.org/10.1016/j.engfracmech.2016.02.045>
- Whitney JM, Nuismer RJ (1974) Stress fracture criteria for laminated composites containing stress concentrations. *J Compos Mater* 8:253–265. <https://doi.org/10.1177/002199837400800303>
- Wu S, Ma J, Cheng Y et al (2018) Numerical analysis of the flattened Brazilian test: failure process, recommended geometric parameters and loading conditions. *Eng Fract Mech* 204:288–305. <https://doi.org/10.1016/j.engfracmech.2018.09.024>
- Zhang X, Sun Z, Hu X (2014) Low temperature fracture toughness of PMMA and crack-tip conditions under flat-tipped cylindrical indenter. *Polym Test* 38:57–63. <https://doi.org/10.1016/j.polymertesting.2014.06.009>

**Publisher's Note** Springer Nature remains neutral with regard to jurisdictional claims in published maps and institutional affiliations.